

See discussions, stats, and author profiles for this publication at: <https://www.researchgate.net/publication/267740303>

# Solid–Solid Phase Transformations Induced through Cation Exchange and Strain in 2D Heterostructured Copper Sulfide Nanocrystals

ARTICLE *in* NANO LETTERS · OCTOBER 2014

Impact Factor: 13.59 · DOI: 10.1021/nl5035607 · Source: PubMed

---

CITATIONS

7

READS

72

## 10 AUTHORS, INCLUDING:



[Don-Hyung Ha](#)

Massachusetts Institute of Technology

14 PUBLICATIONS 263 CITATIONS

[SEE PROFILE](#)



[Robert Hovden](#)

Cornell University

53 PUBLICATIONS 930 CITATIONS

[SEE PROFILE](#)



[Richard G. Hennig](#)

University of Florida

166 PUBLICATIONS 2,180 CITATIONS

[SEE PROFILE](#)



[Richard D Robinson](#)

Cornell University

61 PUBLICATIONS 2,547 CITATIONS

[SEE PROFILE](#)

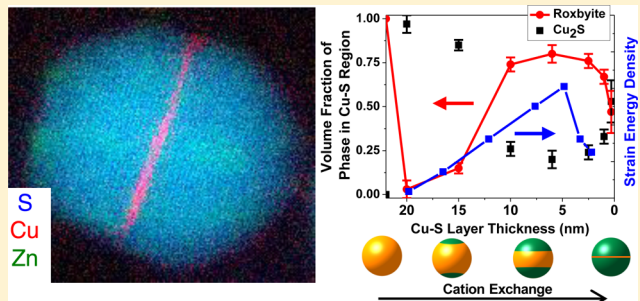
# Solid–Solid Phase Transformations Induced through Cation Exchange and Strain in 2D Heterostructured Copper Sulfide Nanocrystals

Don-Hyung Ha,<sup>†</sup> Andrew H. Caldwell,<sup>†</sup> Matthew J. Ward,<sup>‡</sup> Shreyas Honrao,<sup>†</sup> Kiran Mathew,<sup>†</sup> Robert Hovden,<sup>§</sup> Margaret K. A. Koker,<sup>‡</sup> David A. Muller,<sup>§,||</sup> Richard G. Hennig,<sup>†</sup> and Richard D. Robinson\*,<sup>†</sup>

<sup>†</sup>Department of Materials Science and Engineering, <sup>‡</sup>Cornell High Energy Synchrotron Source (CHESS), <sup>§</sup>School of Applied and Engineering Physics, <sup>||</sup>Kavli Institute at Cornell for Nanoscale Science, Cornell University, Ithaca, New York 14853, United States

## Supporting Information

**ABSTRACT:** We demonstrate dual interface formation in nanocrystals (NCs) through cation exchange, creating epitaxial heterostructures within spherical NCs. The thickness of the inner-disk layer can be tuned to form two-dimensional (2D), single atomic layers (<1 nm). During the cation exchange reaction from copper sulfide to zinc sulfide (ZnS), we observe a solid–solid phase transformation of the copper sulfide phase in heterostructured NCs. As the cation exchange reaction is initiated, Cu ions replaced by Zn ions at the interfaces are accommodated in intrinsic Cu vacancy sites present in the initial roxbyite ( $\text{Cu}_{1.81}\text{S}$ ) phase of copper sulfide, inducing a full phase transition to djurleite ( $\text{Cu}_{1.94}\text{S}$ )/low chalcocite ( $\text{Cu}_2\text{S}$ ), a more thermodynamically stable phase than roxbyite. As the reaction proceeds and reduces the size of the copper sulfide layer, the epitaxial strain at the interfaces between copper sulfide and ZnS increases and is maximized for a copper sulfide disk ~5 nm thick. To minimize this strain energy, a second phase transformation occurs back to the roxbyite phase, which shares a similar sulfur sublattice to wurtzite ZnS. The observation of a solid–solid phase transformation in our unique heterostructured NCs provides a new pathway to control desired phases and an insight into the influence of cation exchange on nanoscale phase transitions in heterostructured materials.



**KEYWORDS:** Cation exchange, diffusion, copper sulfide, plasmonic, phase transformation, 2D heterostructure

**C**ation exchange is a powerful method to postsynthetically manipulate the composition of as-synthesized nanocrystals (NCs).<sup>1</sup> Cation exchange can induce novel NC structural changes, including doping,<sup>2,3</sup> heterostructure formation<sup>4–7</sup> and core–shell formation.<sup>8</sup> The exact mechanistic pathways still remain unknown for nanoscale cation exchange reactions, but certain aspects of the transformation have been empirically determined and qualitative models from minerals and thin-films have been applied to the NC system.<sup>1,9–11</sup>

Cation exchange reactions can act as useful templates to study solid–solid phase transformations in nanoparticles to determine how such processes differ from those in bulk solids. When cations are exchanged from the starting material (parent NC) into the fully exchanged material (child NC), a new phase is often created that is the lowest-energy phase of the fully exchanged material (e.g., wurtzite CdS into orthorhombic  $\text{Ag}_2\text{S}$ ).<sup>1,5</sup> This process is a compositional conversion, not a conventional phase transformation governed by the phase diagram. However, it has recently been shown that the child NC can exist as a stabilized, metastable material either through a partial exchange, such as the formation of a CdS and  $\text{Ag}_2\text{S}$

superlattice,<sup>5</sup> or through a full exchange, such as the formation of  $\text{Cu}_2\text{Se}$  nanocrystals in a metastable hexagonal phase from wurtzite CdSe.<sup>12</sup> Previous research on solid–solid phase transformations in NCs has shown that NCs transform as a single-domain nucleation event,<sup>13,14</sup> that metastable structures can exist in ambient conditions,<sup>15</sup> and that thermodynamic considerations are responsible for the structural metastability rather than the size-dependence of the kinetics.<sup>15</sup> In these solid–solid phase transformation experiments, pressure has been induced in free-standing NCs with exposed surfaces,<sup>13</sup> and these exposed surfaces may influence the transformation; if low index surfaces are dominant then the phase change results in high index, high energy surfaces under high pressure that then act to destabilize the high pressure phase and initiate nucleation of a phase transition. However, if one or more of the surfaces in the nanocrystal are confined, for example, through an epitaxial junction with another crystal, it is unclear how the surface

**Received:** September 15, 2014

**Revised:** October 17, 2014

**Published:** October 22, 2014

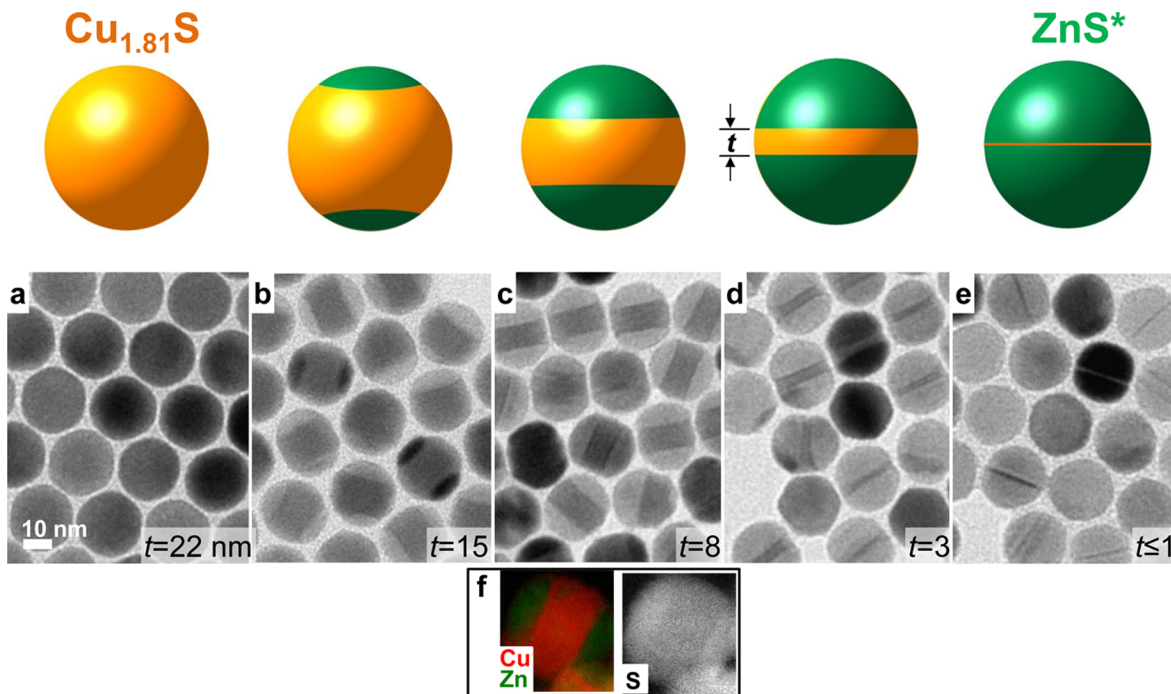


**Figure 1.** Cation exchange transformation of copper sulfide NCs into dual-interface heterostructured particles with zinc sulfide caps. Schematic (top) and TEM images (bottom) show the composition change from the initial copper sulfide particle (a, leftmost) into a ZnS (e, rightmost) with a copper sulfide thin disk. The final product is denoted ZnS\* because a thin 2D copper sulfide disk is present in the TEM images for ~30% of the NCs. The copper sulfide disk thickness ( $t$ ) is indicated. (f) STEM-EELS image showing the presence of Cu and Zn (left) and S (right) in the heterostructured particles.

energies of the free surfaces, the energy of the surface interface, and the effects of diffusion in the crystal will affect the transformation. Little is known about solid–solid transformations in NC heterostructures, specifically how an epitaxial alignment of heterostructures will influence the phase and size of the domain.

Copper sulfide ( $\text{Cu}_{2-x}\text{S}$ ,  $0 \leq x \leq 1$ ) is a p-type semiconductor with potential applications in photovoltaic devices,<sup>16</sup> superionic materials,<sup>17,18</sup> battery electrodes,<sup>19</sup> and photocatalysis.<sup>20</sup> As the properties of copper sulfides are sensitive to both the Cu–S stoichiometry and crystal structures, it is critical to finely tune their phases for use in applications. In addition, copper sulfide is an ideal template material to investigate solid–solid phase transformations because copper sulfide shows unique transformation behaviors such as transient structural transformations under electron-beam irradiation<sup>21</sup> and size dependent solid–solid phase transitions.<sup>22</sup> Heterostructure architectures in NCs enable modulation of electrical and optical properties.<sup>23</sup> In particular, interfacial strain in heterostructures is a key mechanism for controlling electronic band structure,<sup>24</sup> morphology,<sup>5,25</sup> and catalytic activity.<sup>26</sup> Alteration of lattice parameters through lattice mismatch in heterostructures has been widely utilized.<sup>23,24</sup> However, the phase transition induced by lattice strain in free-standing NCs is not well established yet.

In this report, we describe a method to create a dual-interface heterostructure through cation exchange in copper sulfide NCs. We find that cation exchange initially prompts a solid–solid phase transformation in the parent NC copper sulfide phase, transforming it to a lower-energy phase. As the copper sulfide layer becomes thinner it transforms back to the original parent phase due to epitaxial alignment with the child NC material. This is a system in which not only does strain induce a phase

transformation in the NC during cation exchange but also the cation exchange reaction itself initiates a solid–solid phase transformation in the parent NC.

Transmission electron microscopy (TEM) images show the morphology evolution during the transformation (Figure 1,  $t$  = thickness of copper sulfide disk). The initial copper sulfide NCs are spherical with a uniform size (Figure 1a, 22 nm, SD: 3.4%). After the cation exchange reaction is initiated, small ZnS grains symmetrically nucleate on opposite sides of the spherical NCs (Figure 1b). At the onset of ZnS grain growth, the ZnS interfaces curve inward toward the center of the NC (convex ZnS interface). The radius of the interface curvature is ~20 nm at the early stage of the cation exchange reaction when the copper sulfide layer is ~15 nm in thickness (Figure 1b,  $t = 15$  nm). This interface curvature gradually decreases as the cation exchange progresses, with the copper sulfide region in the center of the NCs eventually becoming a disk-like two-dimensional (2D) layer (Figure 1c–e), the thickness of which can be tuned by controlling the reaction time (Table S1, in Supporting Information). These interfaces are stable; the heterostructured NCs retain their interface structure even after a week (Figure S1, in Supporting Information). When the thickness of the copper sulfide layer is ~8 nm (Figure 1c,  $t = 8$  nm) the NCs become slightly elongated perpendicular to the interfaces up to ~10%. At the end of the reaction, most NCs are fully converted to ZnS with the spherical shape and size of the initial copper sulfide NCs preserved; however, approximately 30% of the final NCs maintain a thin copper sulfide layer or show evidence of superimposed lattices from Moire patterns in TEM images of the NCs. The thin copper sulfide layer seen in the center of these NCs disappears during tilting of the TEM specimen holder, suggesting that the value of 30% could be an underestimate of ZnS with copper sulfide disks

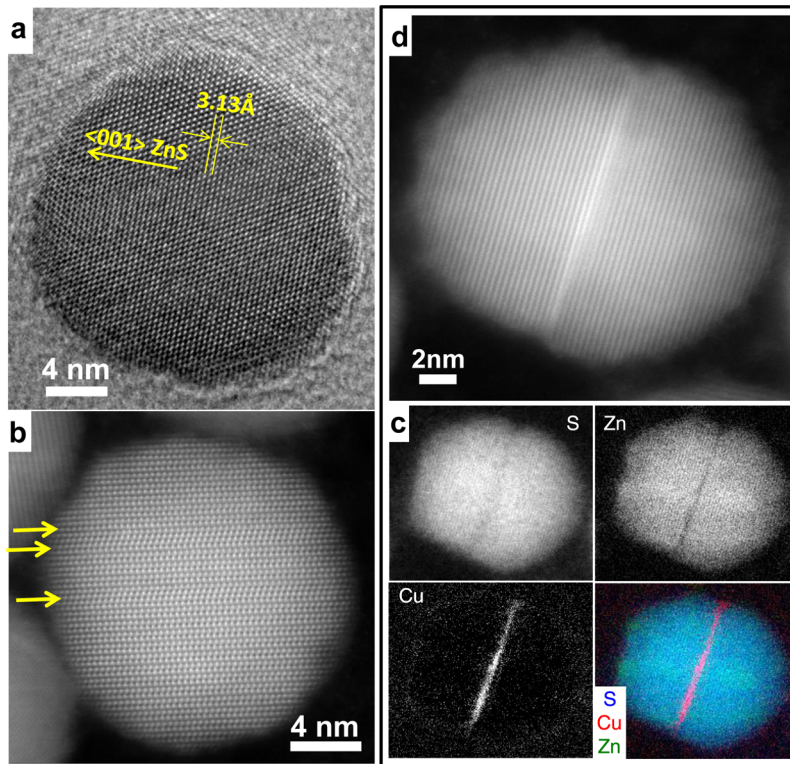


**Figure 2.** HRTEM and STEM images of the cation exchange reaction final sample. (a) HRTEM images show most ZnS\* final sample nanocrystals as perfect crystals without defects. (b) HAADF-STEM image showing stacking faults as indicated by yellow arrows. Approximately 20% of ZnS\* final nanocrystals have stacking faults. (c) EELS mapping verifies the chemical composition of Cu and S in the internal disk region and Zn and S in the surrounding regions. About 30% of the final ZnS NCs show apparent copper sulfide thin disks in the center of nanocrystals indicating that a Cu–Zn–S alloy does not occur. (d) HAADF-STEM of the final samples highlights a near single layer containing Cu.

percentage (see Supporting Information Figure S2). Electron energy loss spectroscopic (EELS) mapping with aberration-corrected scanning transmission electron microscopy (STEM) provides atomic resolution analysis of the chemical structure and confirms that the heterostructured NCs have Zn, Cu, and S elements (Figure 1f). In these “sandwich-like” samples, the electron microscopy study confirms that the two symmetrically growing grains at opposite ends of the NCs are ZnS and that the centrally located “disk” is copper sulfide (Figure 1f).

The final NC sample either resolves into fully crystalline ZnS NCs (estimated at around 70% of the NCs), or NCs with a thin ( $t < 1 \text{ nm}$ ) 2D copper sulfide layer between ZnS grains. For the fully converted ZnS NCs, high-resolution TEM (HRTEM) images indicate good crystallinity with relatively few defects (Figure 2a) and approximately 20% show visible stacking faults (Figure 2b), which may be caused by copper residues. The predominance of final ZnS crystals with low-defects suggests that the dual ZnS growth fronts are well-aligned to the anion sublattice and planar. For the final NCs containing a 2D layer of material, STEM-EELS analysis confirms that the atomically thin layer is composed of Cu and S and that the surrounding material consists of Zn and S (Figure 2c). High-angle annular dark-field scanning transmission electron microscopy (STEM-HAADF) in an aberration-corrected microscope, a technique sensitive to atomic number (Z), is consistent with the EELS data and shows that the high-Z Cu–S layer (appearing as a bright layer in Figure 2d) primarily occupies a single atomic plane in regions but may also extend to adjacent layers. The regions where the Cu concentration width extends two layers may be the result of a planar step viewed in projection or two

adjacent Cu–S layers. That copper sulfide remains in the final NCs for ~30% of the samples indicates there is a stabilization force for the copper sulfide phase even in an aggressive reaction environment. Even Cu–S NCs reacted at higher temperatures for longer times (100 °C for 30 min) also result in ~30% of the final NCs with thin layers (see Supporting Information Figure S3). EELS analysis also suggests that Cu–Zn–S alloy formation does not occur and that a sharp heterostructure interface is maintained in the final NCs. Core–shell structures formed through cation exchange have been studied extensively<sup>9,27</sup> but an atomically thin 2D planar structure centered in a spherical NC has not been achieved previously to our knowledge. This heterostructure formation is not limited to a specific size or shape of copper sulfide NCs. Large (~40 nm) roxbyite NCs of hexagonal bifrustrum shape also transform to 2D heterostructures through this cation exchange reaction (see Supporting Information Figure S4). The ability to create an atomically thin copper sulfide layer in a NC could be useful for examining unique phenomena such as a 2D hole gas, 2D quantum well, or quantized plasmons.<sup>28</sup>

Compared to conventional film deposition techniques such as molecular beam epitaxy (MBE), colloidal nanoparticles present several advantages as a route toward 2D quantum well structures. The relative cost and simplicity of solution-phase syntheses make them attractive from a resources perspective. Solution-phase processing of colloids makes their handling more versatile and enables the industrial-levels of throughput necessary for device fabrication. Colloidal heterostructure NCs exhibit greater flexibility with regards to particle geometry and heterostructure arrangement;<sup>29</sup> traditional thin film fabrication

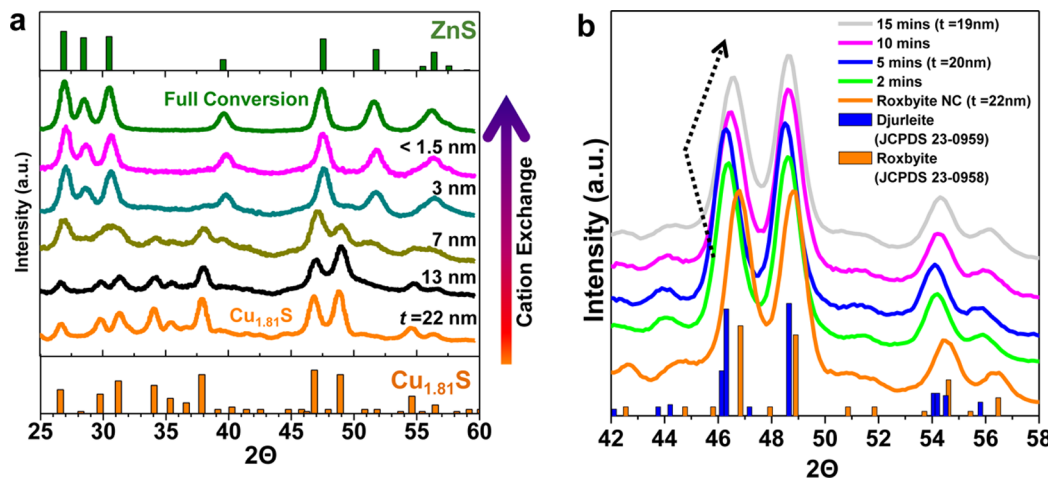


**Figure 3.** XRD structural evolution of heterostructured particles. (a) XRD patterns show the initial particles are well matched to roxbyite phase (a, orange plot and bars) and the phase evolves to ZnS at the conclusion of the reaction (a, green plot and bars). The copper sulfide disk thickness “*t*” maps the progression. Major roxbyite peaks indexed by JCPDS 023-0958 are 26.6 (16 0 0), 29.8 (8 0 4), 31.2 (18 2 1)/(12 8 1), 34.1 (20 0 1)/(10 10 1), 46.8 (0 16 0)/(0 8 6), and 48.9° (8 8 6). Slight variations in plane indices compared to structural analyses in other figures are possible, see Supporting Information. (b) Multiple scans for samples at the early stage of cation exchange reaction from the initial Cu<sub>1.81</sub>S nanocrystals up to the *t* = 19 nm sample. Samples are labeled in terms of the reaction time because the ZnS grains are very small and difficult to quantify until 15 min of the reaction. The 15 min sample corresponds to approximately *t* = 19 nm (ZnS caps grain thickness = ~1.5 nm). The diffraction peaks of the initial roxbyite NC shift to lower 2θ values during the early stages of the reaction (b, 0–15 min) and then shift back to higher 2θ values.

requires the clever manipulation of interfacial strain and surface energies to achieve confined structures beyond large-area planar layers. MBE quantum dots are often limited to shapes such as square pyramidal<sup>29–32</sup> while colloidal nanocrystal heterostructures can have multiple morphologies such as spherical dots, nanorods,<sup>5,33</sup> and branched structures.<sup>5</sup> Moreover, the nature of thin film techniques requires that the nanostructures be attached to a substrate, barring use in *in situ* biological applications such as sensors and labeling.

X-ray diffraction (XRD) patterns of NC samples confirm the chemical transformation from Cu<sub>1.81</sub>S to ZnS (Figure 3a). The XRD pattern of the initial copper sulfide NCs (Figure 3a, orange plot) is well-matched with the roxbyite phase (Figure 3a, orange bars, JCPDS 23-0958), which has ~1.81 (Cu<sub>58</sub>S<sub>32</sub>) stoichiometry between Cu and S atoms.<sup>34,35</sup> Roxbyite has a triclinic crystal structure and is readily synthesized in nanomaterials but is uncommon for bulk syntheses.<sup>34–36</sup> Scherrer analysis of the initial copper sulfide NC’s XRD pattern gives a ~22.5 nm crystallite size, which is consistent with the NC diameter measured from TEM images (~22 nm). (Scherrer analysis was only conducted on the initial and final sample due to complications from overlapping peaks and strain effects in the intermediate heterostructures.) As the extent of cation exchange increases, the XRD contribution from the roxbyite phase gradually decreases, and the ZnS XRD contribution dominates. The peaks corresponding to copper sulfide and ZnS remain distinct during the transformation, suggesting the absence of Cu–Zn–S alloy formation. Interestingly, the XRD peaks corresponding to the initial roxbyite phase show significant shifts toward smaller 2θ angles at the onset of the cation exchange reaction between the initial copper sulfide NCs (*t* = 22 nm) and NCs with small ZnS caps (*t* = ~20 nm) (Figure 3b). The maximum shift toward smaller angles is ~0.5° for the diffraction peaks originally at 48.9 and 46.8° for the 5 min sample, the NCs of which have small ZnS grains (~1 nm thick, *t* = ~20 nm) as measured from TEM images. A shift of this magnitude toward smaller 2θ angles implies that either a phase transition occurs in the copper

sulfide phase or the crystal lattice expands (~1.1% lattice expansion). The shifted peak positions match the reference peak positions of higher Cu-content copper sulfide phases, such as djurleite Cu<sub>1.94</sub>S (Figure 3b) or low-chalcocite Cu<sub>2</sub>S. After the initial shift to smaller 2θ angles, the XRD peaks shift toward larger 2θ angles, indicating that the lattice parameters of the copper sulfide phase are decreasing during cation exchange. Strain is not likely the cause of the shifts toward smaller angles seen in the XRD peaks of Figure 3b because (a) strain from the ZnS interface would move the XRD peaks in the opposite direction to higher angles due to the smaller lattice parameter of ZnS compared to that of roxbyite, (b) there is no broadening of the two major peaks when analyzed by Scherrer (i.e., strain would have to be perfectly homogeneous throughout the copper sulfide, which is unlikely), (c) there is not sufficient ZnS material (<1 nm caps) to create a detectable amount of strain in the copper sulfide, and (d) our continuum modeling indicates negligible strain for these conditions. Therefore, we conclude that the peak shifts in Figure 3b are caused by a phase change from roxbyite to djurleite.

Once larger caps (i.e., *t* < 19 nm) are established, the peak at 48.9° for the initial copper sulfide NCs shifts to 49° for the *t* = 13 nm NC sample and to 49.1° for the *t* = 7 nm NC sample (Supporting Information Figure S5). This peak shifts toward larger 2θ angles and indicates that a ~0.4% lattice contraction occurs for the *t* = 7 nm NCs relative to the initial copper sulfide NCs. When *t* < 7 nm, the XRD signal from ZnS dominates the XRD pattern. The XRD pattern of the final sample is well-matched with that of the wurtzite ZnS phase (Figure 3a, green bars, JCPDS 36-1450), showing no discernible impurity peaks or copper sulfide contributions. The final sample shows a ~23 nm crystallite size, as determined from a Scherrer analysis (see Supporting Information), which is similar to the NC size measured from TEM images (~22 nm, SD: 4%), indicating that the majority of the NCs in the final sample are single crystalline ZnS or have two ZnS grains that are crystallographically well matched as previously seen in stacked nanosheets.<sup>37</sup>

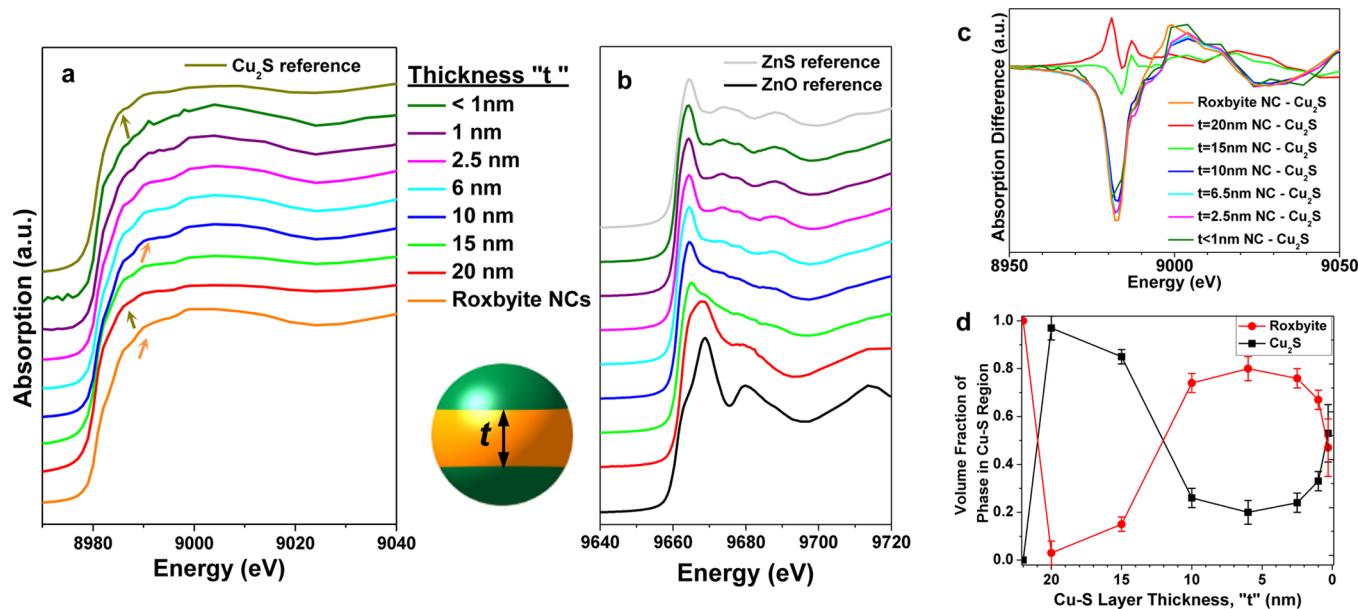


**Figure 4.** XANES structural evolution of heterostructured NCs. XANES measured at Cu (a) and Zn (b) K-edges. As the transformation occurs the thickness of the copper sulfide region decreases, which is indicated in the legend ( $t$ ). The initial copper sulfide roxbyite nanocrystals are shown at the bottom in orange (a). (Note: XANES of the initial roxbyite NCs at the Zn K-edge results in no spectra (b)). Arrows in (a) point out key spectral features of initial roxbyite phase (orange, and orange arrows) and final Cu<sub>2</sub>S phase (top spectra in army green, and army green arrows) that indicate an immediate change in XANES spectra from initial sample to  $t = 20$  sample (red) and then back to roxbyite ( $t = 10$  sample, blue). The reference spectrum for Cu<sub>2</sub>S is shown in (a, army green) and the reference spectra for ZnS and ZnO are shown in (b). During cation exchange, the early nanocrystal samples ( $t = 20$  and 15 nm) exhibit XANES features consistent with Cu<sub>2</sub>S but not of the initial Cu<sub>1.81</sub>S roxbyite phase. (c) Absorption difference of XANES spectra taken between copper sulfide samples and Cu<sub>2</sub>S standard. Early stages of transformation ( $t = 20$  and 15 nm) show high correspondence to Cu<sub>2</sub>S, while other samples more closely match Roxbyite (see Supporting Information). (d) Copper sulfide phase volume fraction as a function of Cu-S layer thickness derived from linear combination fitting of the Cu K-edge XANES using Cu<sub>1.81</sub>S roxbyite (red circles) and Cu<sub>2</sub>S low chalcocite (black squares) phases as reference standards.

X-ray absorption spectroscopy (XAS) provides a complementary approach to XRD for investigating phase transitions in the NCs (Figure 4).<sup>38–40</sup> The high sensitivity and elemental specificity of XAS makes it an ideal method for probing the local chemical environment of complex systems such as our copper sulfide-zinc sulfide heterostructured NCs. In contrast to XRD, which requires long-range order and a reasonably large scattering volume for identification of a minor phase (which may be required to be as large as ~5% of the total volume in order to be detected, depending on the density of scattering atoms and the sample volume), XAS is sensitive to the local chemical environment around an absorber,<sup>41</sup> does not require long-range order (can be measured on amorphous and disordered phases) and is routinely used for chemical speciation and/or phase identification at parts per million (ppm) concentration levels using X-ray fluorescence (XRF) detection methods. Copper and zinc K-edge (1s) X-ray absorption near edge structure (XANES) measurements, which probe the local chemical environment of the Cu or Zn absorber through 1s  $\rightarrow$  np ( $n \geq 4$  for Cu and Zn) dipole allowed ( $\Delta l \pm 1$ ) transitions, were performed on the roxbyite (Cu<sub>1.81</sub>S) NC starting material, NC samples taken from various times during the transformation, and copper (Cu<sub>2</sub>S and CuS) and zinc (ZnS and ZnO) bulk reference standards.

The Cu K-edge XANES of NC samples with various copper sulfide layer thicknesses,  $t$ , from the initial roxbyite starting material to the final NC sample, as well as that for the Cu<sub>2</sub>S bulk reference standard are displayed in Figure 4a. A shift in the Cu K-edge toward a XANES spectrum exhibiting spectral features of Cu<sub>2</sub>S (Figure 4a and Supporting Information Figure

S6, S7) was observed immediately (5 min) after the chemical transformation begins. The copper K-edge XANES of NC samples with  $t = 20$  and 15 nm exhibit XANES profiles of Cu<sub>2</sub>S (djurleite/low chalcocite) in the near-edge region.<sup>42,43</sup> After 50 min (when the thickness of the copper sulfide band in the NC,  $t$ , is 10 nm) the Cu K-edge XANES shifts back to that of the initial roxbyite NC starting material (see Figure 4a and Supporting Information Figures S6 and S8). This phase transformation from Cu<sub>1.81</sub>S (roxbyite) to Cu<sub>2</sub>S and back to Cu<sub>1.81</sub>S is clearly shown if we take the difference between the Cu<sub>2</sub>S standard XANES spectra and the spectra of each of the various time slices from the chemical transformation (Figure 4c and Supporting Information Figure S9). The difference spectra between each time slice and the initial roxbyite phase are shown in Supporting Information Figure S9. All NC samples with  $t \leq 10$  nm appear to exhibit the XANES profile of the initial roxbyite phase (note: initial roxbyite NC size is  $t = 22$  nm). The Cu K-edge XANES of the final NC sample ( $t < 1$  nm), although noisy due to the very low concentration of copper remaining in the sample, appears to have a similar spectral profile to the roxbyite phase.

We postulate that there remains a small amount of the roxbyite phase in the copper sulfide disk of the heterostructure after the transformation to djurleite/low chalcocite. In order to test this, and to quantify Cu<sub>1.81</sub>S and Cu<sub>2</sub>S contributions to the copper K-edge XANES of the heterostructure NCs, we fit the absorption coefficient,  $\mu(E)$ , with a linear combination of Cu<sub>1.81</sub>S (roxbyite) and Cu<sub>2</sub>S (djurleite/low chalcocite) reference spectra (see Figure S10 and Table S2 and discussion that follows in Supporting Information). LC (Linear combina-

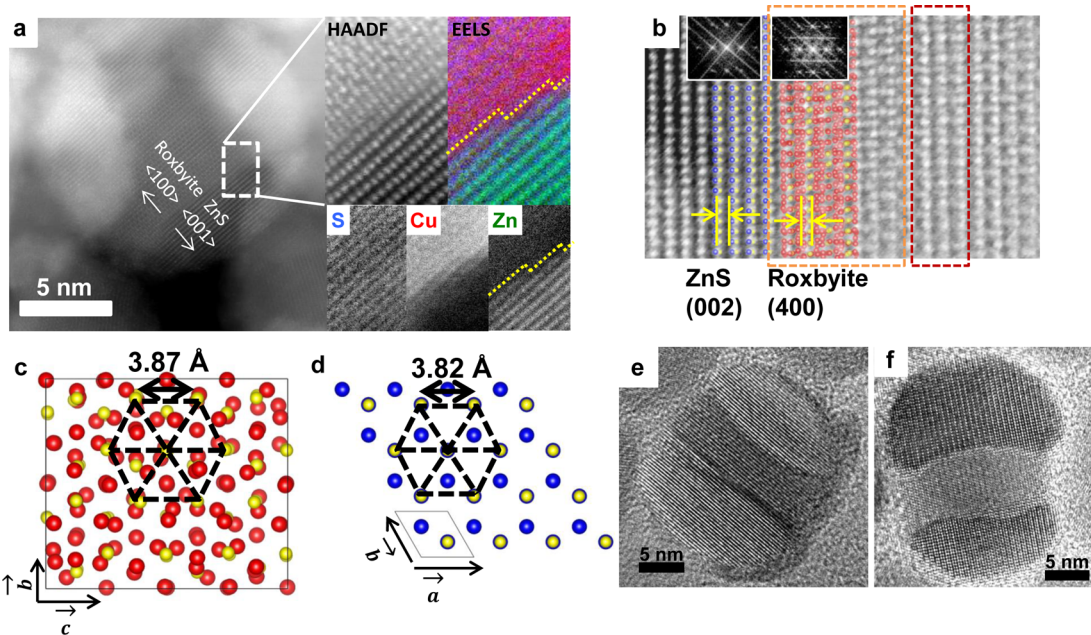


**Figure 5.** Characterization of the heterointerface. (a) STEM images (HAADF and EELS) images of the interface showing the elemental composition and atomic steps (yellow dotted line). (b) HRTEM image of a nanocrystal with a thick copper sulfide layer ( $\sim 12$  nm) showing the epitaxial interface of the roxbyite to the ZnS, and stacking faults in the copper sulfide further away from the interface. (c,d) Atomic models of the roxbyite (c) and ZnS (d) lattices. The sulfur atoms are shown in yellow. The sulfur sublattice has a good epitaxial match between the two structures with only 1.1% mismatch for the (100) and (001) planes in the roxbyite and ZnS, respectively. (e,f) HRTEM images showing the convex curvature of ZnS caps (e) and concave curvature of CdS caps (f) on the copper sulfide layer. The opposite curvature is due to the reversal of interfacial strain for the ZnS (copper sulfide is in compression) versus the CdS (copper sulfide is in tension) caps.

tion)-XANES fitting of Cu K-edge XANES profiles from the NC samples indicate that upon initial formation of ZnS grains (initial ZnS-Cu<sub>1.81</sub>S-ZnS heterostructure,  $t = 20$  nm) the copper sulfide phase undergoes a rapid and nearly complete transformation from Cu<sub>1.81</sub>S (roxbyite) to a Cu<sub>2</sub>S (low chalcocite/djurleite) phase (see Figure 4d and Supporting Information Table S2). The solid–solid copper sulfide phase transformation indicated by the XANES analysis corroborates XRD results that show a peak shift toward smaller  $2\theta$  angles observed in the initial transformed NC samples ( $22 > t > 13$  nm) (Figure 3b) and thus confirms the solid–solid phase transformation of copper sulfide during the cation exchange reaction. As the cation exchange proceeds and the relative volume fraction of copper sulfide to ZnS in the NCs decreases, the phase fraction of Cu<sub>1.81</sub>S increases until it reaches a maximum for the sample  $t = 6$  nm (Figure 4d and Supporting Information Table S2). The position of  $E_0$  (absorption edge) for the heterostructured NC samples, the Cu<sub>1.81</sub>S roxbyite NC starting materials, and the Cu<sub>2</sub>S bulk sample was  $\sim 8980$  eV (Supporting Information Table S3), which is consistent with copper in the 1+ oxidation state ( $E_0$  for Cu metal is 8979 eV).

Zinc K-edge XANES of the heterostructured NC samples as well as those of the ZnS and ZnO reference standards are shown in Figure 4b. The  $t = 20$  nm NC sample has strong contributions from both ZnS and ZnO. The ZnO contribution can be attributed to air-oxidation of ZnS after the NCs have been synthesized. Because there is only a very thin ZnS capping layer ( $\sim 1$  nm) at the poles of the NC in the initially transformed sample ( $t = 20$  nm sample in Figure 4b), the amorphous ZnO layer on the surface dominates the absorption spectrum. As the volume fraction of ZnS in the NCs increases, contributions to the Zn K-edge XANES spectrum from the ZnO surface oxide layer rapidly decrease. For NC samples with

$t < 2.5$  nm the spectral features of the near edge region become increasingly sharp as the crystallinity of ZnS increases. The position of  $E_0$  for the samples with  $t < 15$  nm, the bulk ZnS and the bulk ZnO is  $\sim 9661$  eV (Supporting Information Table S4), which is consistent with zinc in the 2+ oxidation state ( $E_0$  for Zn metal is 9659 eV). The position of  $E_0$  for the sample with  $t = 20$  nm is  $9662.3 \pm 0.1$  eV, but this increase is most likely the result of the superposition of  $\mu(E)$  contributions from ZnO and ZnS and does not reflect a change in the oxidation state of Zn. This slight shift of  $E_0$  to higher energy decreases with an increase in the ZnS contribution to  $\mu(E)$  as the cation exchange proceeds, which is consistent with the preceding argument.

To understand the solid–solid phase transformation in the copper sulfide layer it is necessary to examine the interface between ZnS and copper sulfide. HAADF and HRTEM characterization reveals that the copper sulfide–zinc sulfide heterostructure interface is atomically sharp (Figure 5a,b), implying that Cu ions and Zn ions do not interdiffuse and that cation exchange only occurs at the interface. The crystallographic planes along the interface were identified as (100/100) (corresponding to ⟨100⟩) for roxbyite and (001/001) (corresponding to ⟨001⟩) for ZnS, based on the spacing of the planes and the Fourier transform of the lattices at the interface, as shown in the HAADF and HRTEM images (Figure 5a,b and Supporting Information Figure S11). These epitaxial interfaces form due to the well-matched sulfur sublattices shared by Cu<sub>1.81</sub>S (triclinic, space group P $\bar{1}$ ) and wurtzite ZnS (space group P6<sub>3</sub>mc) (Figure 5c,d). Although roxbyite copper sulfide has a low symmetry crystal structure, its sulfur sublattice for (001/001) is hexagonal with maximum deviations of  $\pm 0.35$  Å from the sulfur sublattice spacing in wurtzite ZnS (001/001) (Supporting Information Figure S12). In addition, dual interface formation in our Cu<sub>1.81</sub>S/ZnS heterostructured NCs

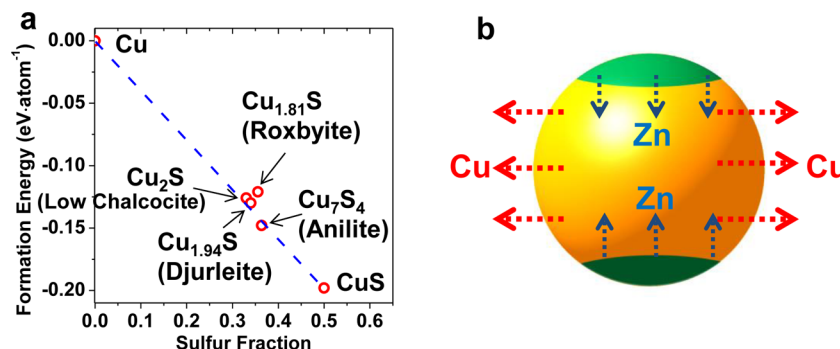


**Figure 6.** Phase stability calculation and diffusion pathways. (a) Formation energy calculations of copper sulfide phases. (b) The diffusion pathways of Cu and Zn atoms during the cation exchange reaction in heterostructured nanocrystals. On the basis of calculated diffusion activation barriers, during the cation exchange the Zn diffuses inward from the ZnS regions (green) and the Cu diffuses in the Cu–S region (orange). The excess Cu in the Cu–S region could be the cause for the solid–solid phase transformation.

may be due to similar atomic arrangements of the (100) and ( $\bar{1}00$ ) plane of the roxbyite phase, which provides a similar chemical environment for the cation exchange and interface formation (see Supporting Information Figure S13). However, other planes are poorly matched between low symmetry roxbyite and wurtzite ZnS (see Supporting Information Figure S14). This favorable epitaxial matching with only a few atomic planes is likely the reason that Cu<sub>1.81</sub>S/ZnS heterostructured NCs do not form a core–shell structure. This dual interface formation is different from previous reports of CdS–Cu<sub>2</sub>S that cite the two atomically distinct crystal planes of (001) and (00 $\bar{1}$ ) as leading to different reactivities at either end of the CdS nanorod for forming either one or two interfaces.<sup>4</sup> The lattice constant of the sulfur sublattice in ZnS (001/00 $\bar{1}$ ) is 1.1% smaller than that of the sulfur sublattice in roxbyite (100/ $\bar{1}00$ ). This lattice mismatch results in the formation of curved interfaces between copper sulfide and ZnS (Figure 5e); strain relaxation occurs by the development of atomic steps along the interfaces (Figure 5a, yellow dotted lines show the atomic steps between copper sulfide and ZnS). This curvature can be engineered by reversing the stress at the interface, for example, by using Cd rather than Zn in the cation exchange reaction to form CdS, which has a sulfur sublattice spacing that is 6.8% larger than that of roxbyite copper sulfide (Figure 5f). This lattice mismatch induces interface formation with an outward curvature that is opposite to that of the interface between copper sulfide and ZnS. HRTEM images of the interface confirm that the roxbyite phase is stabilized epitaxially at the ZnS surface; however, further into the copper sulfide region there are stacking faults that may indicate the presence of different Cu–S phases (Figure 5b).

Density functional theory (DFT) has been extensively used to study the thermodynamic stability of different phases and to predict the lowest energy structures.<sup>39,44</sup> DFT calculations predict that the phase transition from roxbyite to copper-rich phases such as djurleite and low chalcocite during the chemical transformation is thermodynamically favorable (Figure 6a). Our calculation of diffusion activation barriers indicate that Cu ions diffuse much faster in the roxbyite phase than in ZnS or CdS (see Table 1). In addition, the diffusion activation barriers for Zn and Cd are smaller in ZnS and CdS, respectively, than in roxbyite. By taking into consideration these calculated diffusion activation barriers, an accurate picture of the cation exchange process can be formed. Zn ions participating in the cation exchange reaction at the Cu<sub>1.81</sub>S/ZnS interface are supplied from the Zn ion solution and diffuse through the ZnS phase,

**Table 1. Diffusion Activation Barrier for Cu, Zn, and Cd**

diffusing atom	diffusion activation barrier (eV)		
	in roxbyite	in ZnS	in CdS
Cu	0.08	1.21	0.37
Zn	0.54	0.35	
Cd	0.86		0.22

whereas the Cu ions replaced by the Zn ions are released into the solution via diffusion through the copper sulfide region as shown in Figure 6b. During this diffusion of Cu outward into the solution, a fraction of the Cu ions are accommodated in intrinsic Cu vacancy sites present in the roxbyite phase, inducing a phase transition to the more Cu-rich copper sulfide phases such as djurleite or low chalcocite. Djurleite and low chalcocite are more thermodynamically stable phases than roxbyite (Figure 6a); roxbyite has a formation energy of -0.12 eV per atom, while djurleite (Cu<sub>1.94</sub>S) and low chalcocite (Cu<sub>2</sub>S) have lower formation energies (-0.126 eV for djurleite and -0.13 eV for low chalcocite) and share a similar crystal structure with a slightly higher Cu to S ratio. The anion sublattice framework should be preserved during this phase transition between copper sulfide phases as well as between the zinc and copper sulfide cation exchange; the concept of anion sublattice preservation during cation exchange has been previously documented.<sup>45</sup> Thus, it is a thermodynamic driving force that induces the copper sulfide phase transition in the early stages of the cation exchange reaction as confirmed by XRD and XANES (Figures 3b and 4c,d).

The findings from continuum modeling calculations of the strain distributions in the heterostructured NCs corroborate the NC morphology evolution seen during cation exchange (Figure 7).<sup>46</sup> The calculated direction of the interfacial curvature between ZnS/CdS and Cu<sub>1.81</sub>S agrees with the experimentally observed interfacial curvature (ZnS–Cu<sub>1.81</sub>S, curved inward to the center copper sulfide layer; CdS–Cu<sub>1.81</sub>S, curved outward from the center copper sulfide layer). The strain along the axis perpendicular to the interfaces (z-direction, Figure 7a, bottom) determines the curvature. The z-direction strain arises from the mismatched interfacial strain along the x-direction (the y-direction has the same degree of strain as the x-direction due to isotropic strain along the xy-plane). The difference (~1.1%) in the z-direction strain between the center of the NC and outer surface of the copper sulfide layer leads to an inward curvature of the interface toward the center (compressive strain in the center and tensile strain at the sides of the copper sulfide layer).

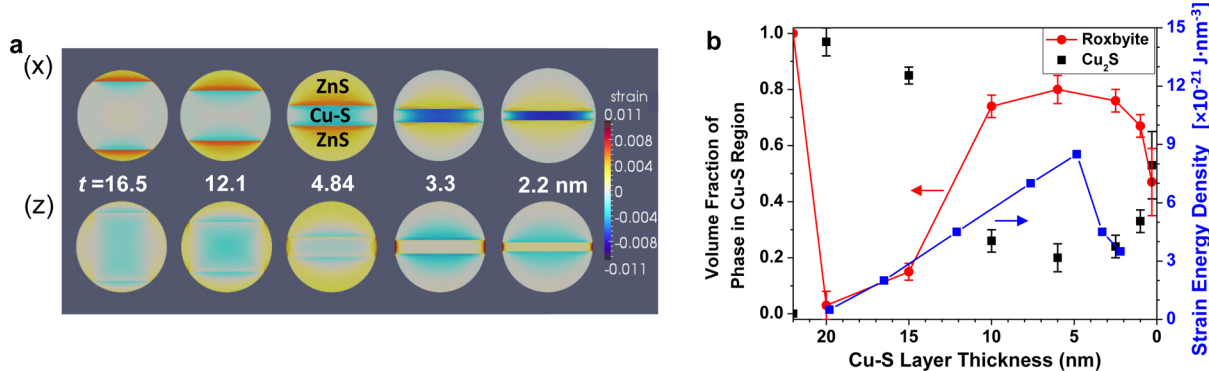


**Figure 7.** Modeled strain in the heterostructured nanocrystals. (a, top) Strain for the  $x$ - $y$  direction, parallel to the interface. (a, bottom) Strain for the  $z$ -direction, perpendicular to the interface. The color scale spans from 1.1% compression (red) to 1.1% tension (dark blue). (b) Strain energy density (blue squares, right  $y$ -axis) found from strain model and plotted against phase fraction in the copper sulfide. As the total strain in the nanocrystal increases the majority of the copper sulfide phase reverts to roxbyite, which has a good epitaxial match to the ZnS interface.

The calculated strain energy density in a NC during cation exchange increases as the copper sulfide layer thickness decreases (Figure 7b, blue points, right-hand  $y$ -axis). The strain energy density increases as the cation exchange reaction progresses, and is a maximum ( $8.5 \times 10^{-21} \text{ J}\cdot\text{nm}^{-3}$ ) when  $t = 4.8 \text{ nm}$ . The strain energy gradually decreases as the copper sulfide layer thickness decreases further ( $t < 4.8 \text{ nm}$ ).

It is likely that the evolution of the strain energy density in our heterostructured NCs is directly linked to the copper sulfide phase transitions characterized through XAS. Because the lattice of the roxbyite phase is better-matched to the sulfur sublattice of ZnS at the interface than that of djurleite/low chalcocite (see Supporting Information Figures S12, S15, and S16), the roxbyite phase is strain-stabilized at the interfaces. As the thickness of the copper sulfide layer decreases, the djurleite phase that is present in the NC interior, away from the interfaces, transforms to roxbyite to minimize lattice strain, even though djurleite/low chalcocite in bulk is thermodynamically more stable than roxbyite. The evolution of the calculated strain energy mirrors the phase transitions determined from the XANES fitting. XANES analysis shows that the initial NC is entirely of the roxbyite phase of copper sulfide, and that, at the onset of the cation exchange reaction, the majority (97%) of the copper sulfide volume immediately transforms to the low chalcocite/djurleite phase (Figure 7b, red and black points). As the reaction proceeds, the volume fraction of the roxbyite phase gradually increases until the thickness of the copper sulfide layer is 6 nm ( $t = 6 \text{ nm}$ ); this trend is well-matched with the strain energy calculation, which shows that the strain energy reaches a maximum at  $t = 5 \text{ nm}$ . During the transformation, the roxbyite phase is stabilized at the ZnS interface as a consequence of minimizing interfacial strain. HAADF images confirm that the copper sulfide phase at the interface with ZnS is Cu<sub>1.81</sub>S (roxbyite), while stacking faults observed in the middle of the copper sulfide region indicate the presence of different copper sulfide compositions (Figure 5b). The strain controlled phase transition in copper sulfide NCs suggests that this roxbyite phase should appear at the interface with other wurtzite metal sulfides where the properties of heterostructures are controlled.

This result is interesting in light of previous research on solid–solid phase transformations in NCs. Previous work has demonstrated that the entire NC acts as a single domain for phase transitions under high pressure.<sup>47</sup> Other work has attempted to identify the critical nucleus for phase trans-

formations through a 1D nucleation seed.<sup>48</sup> These results are based on free-standing NCs with pressure-induced transformations. Our result shows a coexistence of two phases within the Cu–S layer of the NC. However, a clear trend in the initial transformation indicates that the NC would prefer to transform as a single domain (NC transforms to djurleite/low chalcocite upon initiation of the cation exchange). A single-domain transformation is supported by the fact that (a) XANES data shows over a 95% transformation to djurleite at the onset and (b) in XRD we see no peak broadening or splitting for the major peaks at  $\sim 47$  and  $\sim 49^\circ$ . However, the second phase transition induced by lattice strain does not appear to prefer a single domain even though the thickness of the Cu–S region is only between 1 and 10 nm. This may imply that the critical nucleus for the phase transition mediated by cation exchange is different from that mediated by interfacial strain. In addition, the phase transformations back and forth between roxbyite and djurleite/low chalcocite is energetically similar to the transient transformations between the low chalcocite and high chalcocite phase observed by TEM.<sup>21</sup> The calculated formation energies per formula unit between roxbyite and djurleite/low chalcocite are 42 meV/38 meV, which are comparable with that between low chalcocite and high chalcocite (40 meV);<sup>21,49</sup> however, in the roxbyite and djurleite/low chalcocite case one would expect a progression to the lower energy phase (djurleite/low chalcocite) and a larger barrier for a reverse transform.

The heterostructured NCs exhibit localized surface plasmon resonance (LSPR) peaks due to the intrinsically high carrier concentration of copper sulfide (Figure 8). Cu<sub>2-x</sub>S is a well-known p-type semiconductor exhibiting a stoichiometry-dependent bandgap.<sup>50,51</sup> By controlling the extent of cation exchange between copper sulfide and ZnS the resonance wavelength of the surface plasmons in the copper sulfide phase of our NCs can be tuned over a broad range of wavelengths from  $\sim 1300 \text{ nm}$  for the initial copper sulfide NCs to  $\sim 2300 \text{ nm}$  for the NCs with a thin ( $t = 2 \text{ nm}$ ) copper sulfide layer. Several mechanisms may account for the LSPR redshift resulting from the cation exchange reaction. First, the copper sulfide hole concentration is dependent on the stoichiometry, and thus transitions from roxbyite to more copper-rich phases will decrease the carrier concentration, resulting in a redshift in the plasmon resonance.<sup>52</sup> Second, changes in the copper sulfide structure due to a phase change or strain in the lattice may alter the dielectric constant or free hole effective mass, both of which

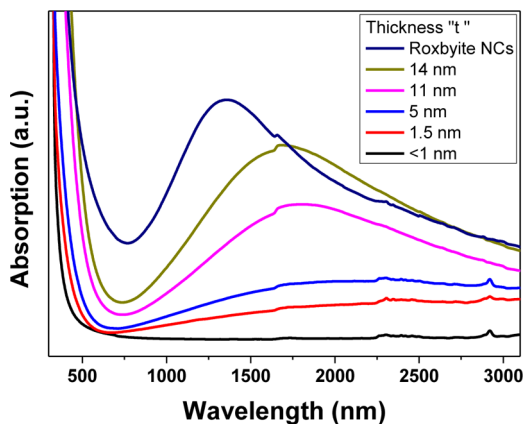


**Figure 8.** Absorption spectra of nanocrystal samples. The initial roxybite  $\text{Cu}_{1.81}\text{S}$  nanocrystals (dark blue line) show LSPR peak at  $\sim 1300$  nm. The LSPR peak shifts toward longer wavelength with decreasing thickness ( $t$ ) of the copper sulfide layer confined between ZnS caps. The final nanocrystal sample (black line) does not exhibit an LSPR peak.

would cause a plasmon resonance wavelength shift; however, both parameters have to change by more than 3 times their original values to result in the LSPR redshifts measured for our samples (3 times higher effective mass or 3 times lower dielectric constant than the initial copper sulfide NCs), considering only the properties of roxybite copper sulfide. Such large changes in the free hole effective mass or dielectric constant are not possible for this system even if one considers the effects of lattice strain, as DFT calculations show that the NC lattice strains will only induce only a few percent change in the dielectric constant and effective mass. Lastly, as the volume fraction of copper sulfide decreases, the dielectric constant of ZnS becomes increasing influential regarding the electronic properties of the NC. The LSPR redshift could therefore result from increasing the dielectric constant of the local medium surrounding the copper sulfide phase via the growth of the ZnS grains. Overall, the plasmon resonance redshift is most likely the result of a decrease in the carrier concentration and an enlargement in the surrounding dielectric material, but these conclusions warrant further study. We have recently developed an analytical model in an attempt to replicate the LSPR shifts for these heterostructures.<sup>53</sup>

In this study, we demonstrated the synthesis of dual-interface, heterostructured NCs through cation exchange. The heterostructure consists of a copper sulfide layer capped with zinc sulfide grains in spherical NCs and can be tuned by controlling the extent of the cation exchange reaction. The reaction can produce an atomic layer of 2D copper sulfide within a ZnS NC with epitaxial connections between the two materials, which provides a template to investigate unique phenomena in NCs, such as a 2D hole gas or 2D quantum well. In the early stage of the reaction, we observe a solid–solid phase transition of the copper sulfide phase from roxybite to a more thermodynamically stable, copper-rich phase (djurleite/low chalcocite). This first phase transformation occurs as a result of copper ions, displaced by Zn ions, occupying the intrinsic vacancy sites of the roxybite phase. The minimization strain energy induces a second phase transition back to roxybite, which forms a better-matched epitaxial interface with zinc sulfide than does djurleite or low chalcocite. The strain-controlled phase transformation in free-standing copper sulfide

NCs implies that this roxybite phase may appear at the interface with other wurtzite metal sulfides where the properties of heterostructures are determined. This solid–solid phase transition provides insights to understand and control the nucleation of phase transformations in nanoscale systems with two different types (cation exchange and interfacial strain) of origins triggering a phase transition.

## ■ ASSOCIATED CONTENT

### S Supporting Information

Sample synthesis and characterization methods; additional cation exchange reaction results; continuum model and density functional theory calculations; XANES analysis; and STEM and EELS analysis. This material is available free of charge via the Internet at <http://pubs.acs.org>.

## ■ AUTHOR INFORMATION

### Corresponding Author

\*E-mail: rdr82@cornell.edu.

### Notes

The authors declare no competing financial interest.

## ■ ACKNOWLEDGMENTS

We thank Rong Huang, Darren Dale, and Ken Finkelstein for their assistance with the experimental setup at CHESS. We also thank Francis DiSalvo for helpful comments. This work made use of the Cornell Center for Materials Research Shared Facilities which are supported through the NSF MRSEC program (DMR-1120296). The work was supported in part by the National Science Foundation under Award Number CHE-1152922. The Cornell High Energy Synchrotron Source (CHESS) is supported by the NSF & NIH/NIGMS via NSF award DMR-0936384. D-H.H., S.H., K.M., R.G.H., and R.D.R. were supported as part of the Energy Materials Center at Cornell (EMC<sup>2</sup>), an Energy Frontier Research Center funded by the U.S. Department of Energy, Office of Science, Office of Basic Energy Science under Award Number DE-SC0001086. This research used computational resources of the Texas Advanced Computing Center under Contract No. TG-DMR050028N and of the Computation Center for Nanotechnology Innovation at Rensselaer Polytechnic Institute.

## ■ REFERENCES

- (1) Son, D. H.; Hughes, S. M.; Yin, Y. D.; Alivisatos, A. P. *Science* **2004**, *306*, 1009–1012.
- (2) Sahu, A.; Kang, M. S.; Komphch, A.; Notthoff, C.; Wills, A. W.; Deng, D.; Winterer, M.; Frisbie, C. D.; Norris, D. J. *Nano Lett.* **2012**, *12* (5), 2587–2594.
- (3) Vlaskin, V. A.; Barrows, C. J.; Erickson, C. S.; Gamelin, D. R. *J. Am. Chem. Soc.* **2013**, *135* (38), 14380–14389.
- (4) Sadtler, B.; Demchenko, D. O.; Zheng, H.; Hughes, S. M.; Merkle, M. G.; Dahmen, U.; Wang, L.-W.; Alivisatos, A. P. *J. Am. Chem. Soc.* **2009**, *131* (14), 5285–5293.
- (5) Robinson, R. D.; Sadtler, B.; Demchenko, D. O.; Erdonmez, C. K.; Wang, L. W.; Alivisatos, A. P. *Science* **2007**, *317* (5836), 355–358.
- (6) Demchenko, D. O.; Robinson, R. D.; Sadtler, B.; Erdonmez, C. K.; Alivisatos, A. P.; Wang, L. W. *ACS Nano* **2008**, *2* (4), 627–636.
- (7) Manna, L.; Scher, E. C.; Alivisatos, A. P. *J. Am. Chem. Soc.* **2000**, *122* (51), 12700–12706.
- (8) Sytnyk, M.; Kirchschlager, R.; Bodnarchuk, M. I.; Primetzhofer, D.; Kriegner, D.; Enser, H.; Stangl, J.; Bauer, P.; Voith, M.; Hassel, A. W.; Krumeich, F.; Ludwig, F.; Meingast, A.; Kothleitner, G.; Kovalenko, M. V.; Heiss, W. *Nano Lett.* **2013**, *13* (2), 586–593.

- (9) Beberwyck, B. J.; Surendranath, Y.; Alivisatos, A. P. *J. Phys. Chem. C* **2013**, *117* (39), 19759–19770.
- (10) Putnis, A. *Mineral. Mag.* **2002**, *66* (5), 689–708.
- (11) Fedorov, V. A.; Ganshin, V. A.; Korkishko, Y. N. *Phys. Status Solidi A* **1993**, *139* (1), 9–65.
- (12) Li, H.; Zanella, M.; Genovese, A.; Povia, M.; Falqui, A.; Giannini, C.; Manna, L. *Nano Lett.* **2011**, *11* (11), 4964–4970.
- (13) Tolbert, S. H.; Alivisatos, A. P. *Science* **1994**, *265* (5170), 373–376.
- (14) Jacobs, K.; Zaziski, D.; Scher, E. C.; Herhold, A. B.; Paul Alivisatos, A. *Science* **2001**, *293* (5536), 1803–1806.
- (15) Jacobs, K.; Wickham, J.; Alivisatos, A. P. *J. Phys. Chem. B* **2002**, *106* (15), 3759–3762.
- (16) Wu, Y.; Wadia, C.; Ma, W.; Sadtler, B.; Alivisatos, A. P. *Nano Lett.* **2008**, *8* (8), 2551–2555.
- (17) Wakamura, K. *Solid State Ionics* **2002**, *149* (1–2), 73–80.
- (18) Miller, T.; Wittenberg, J.; Wen, H.; Connor, S.; Cui, Y.; Lindenberg, A. *Nat. Commun.* **2013**, *4*, 1369.
- (19) Lai, C.-H.; Huang, K.-W.; Cheng, J.-H.; Lee, C.-Y.; Hwang, B.-J.; Chen, L.-J. *J. Mater. Chem.* **2010**, *20* (32), 6638–6645.
- (20) Cheng, Z.; Wang, S.; Wang, Q.; Geng, B. *CrystEngComm* **2010**, *12* (1), 144–149.
- (21) Zheng, H.; Rivest, J. B.; Miller, T. A.; Sadtler, B.; Lindenberg, A.; Toney, M. F.; Wang, L.-W.; Kisielowski, C.; Alivisatos, A. P. *Science* **2011**, *333* (6039), 206–209.
- (22) Rivest, J. B.; Fong, L.-K.; Jain, P. K.; Toney, M. F.; Alivisatos, A. P. *J. Phys. Chem. Lett.* **2011**, *2* (19), 2402–2406.
- (23) Donega, C. d. M. *Chem. Soc. Rev.* **2011**, *40* (3), 1512–1546.
- (24) Smith, A. M.; Mohs, A. M.; Nie, S. *Nat. Nanotechnol.* **2009**, *4* (1), 56–63.
- (25) McDaniel, H.; Zuo, J.-M.; Shim, M. *J. Am. Chem. Soc.* **2010**, *132* (10), 3286–3288.
- (26) Wu, J.; Li, P.; Pan, Y.-T.; Warren, S.; Yin, X.; Yang, H. *Chem. Soc. Rev.* **2012**, *41* (24), 8066–8074.
- (27) Rivest, J. B.; Jain, P. K. *Chem. Soc. Rev.* **2013**, *42* (1), 89–96.
- (28) Scholl, J. A.; Koh, A. L.; Dionne, J. A. *Nature* **2012**, *483* (7390), 421–427.
- (29) Leon, R.; Petroff, P. M.; Leonard, D.; Fafard, S. *Science* **1995**, *267* (5206), 1966–1968.
- (30) Grundmann, M.; Christen, J.; Ledentsov, N. N.; Böhrer, J.; Bimberg, D.; Ruvimov, S. S.; Werner, P.; Richter, U.; Gösele, U.; Heydenreich, J.; Ustinov, V. M.; Egorov, A. Y.; Zhukov, A. E.; Kop'ev, P. S.; Alferov, Z. I. *Phys. Rev. Lett.* **1995**, *74* (20), 4043–4046.
- (31) Leonard, D.; Krishnamurthy, M.; Reaves, C. M.; Denbaars, S. P.; Petroff, P. M. *Appl. Phys. Lett.* **1993**, *63* (23), 3203–3205.
- (32) Tersoff, J.; Tromp, R. M. *Phys. Rev. Lett.* **1993**, *70* (18), 2782–2785.
- (33) Milliron, D. J.; Hughes, S. M.; Cui, Y.; Manna, L.; Li, J.; Wang, L.-W.; Paul Alivisatos, A. *Nature* **2004**, *430* (6996), 190–195.
- (34) Mumme, W.; Sparrow, G.; Walker, G. *Mineral. Mag.* **1988**, *52* (366), 323–330.
- (35) Mumme, W. G.; Gable, R. W.; Petříček, V. *Can. Mineral.* **2012**, *50* (2), 423–430.
- (36) Saldanha, P. L.; Brescia, R.; Prato, M.; Li, H.; Povia, M.; Manna, L.; Lesnyak, V. *Chem. Mater.* **2014**, *26* (3), 1442–1449.
- (37) Aksit, M.; Toledo, D. P.; Robinson, R. D. *J. Mater. Chem.* **2012**, *22* (13), 5936–5944.
- (38) Ward, M. J.; Han, W.-Q.; Sham, T.-K. *J. Phys. Chem. C* **2013**, *117* (39), 20332–20342.
- (39) Ha, D.-H.; Moreau, L. M.; Bealing, C. R.; Zhang, H.; Hennig, R. G.; Robinson, R. D. *J. Mater. Chem.* **2011**, *21* (31), 11498–11510.
- (40) Moreau, L. M.; Ha, D.-H.; Zhang, H.; Hovden, R.; Muller, D. A.; Robinson, R. D. *Chem. Mater.* **2013**, *25* (12), 2394–2403.
- (41) Moreau, L. M.; Ha, D.-H.; Bealing, C. R.; Zhang, H.; Hennig, R. G.; Robinson, R. D. Unintended Phosphorus Doping of Nickel Nanoparticles during Synthesis with TOP: A Discovery through Structural Analysis. *Nano Letters* **2012**, *12*, 4530–4539.
- (42) Patrick, R. A. D.; Mosselmans, J. F. W.; Charnock, J. M.; England, K. E. R.; Helz, G. R.; Garner, C. D.; Vaughan, D. J. *Geochim. Cosmochim. Acta* **1997**, *61* (10), 2023–2036.
- (43) Etschmann, B.; Liu, W.; Testemale, D.; Mueller, H.; Rae, N.; Proux, O.; Hazemann, J.-L.; Brugger, J. *Geochim. Cosmochim. Acta* **2010**, *74* (16), 4723–4739.
- (44) Kim, J. C.; Moore, C. J.; Kang, B.; Hautier, G.; Jain, A.; Ceder, G. *J. Electrochem. Soc.* **2011**, *158* (3), A309–A315.
- (45) Jain, P. K.; Amirav, L.; Aloni, S.; Alivisatos, A. P. *J. Am. Chem. Soc.* **2010**, *132* (29), 9997–9999.
- (46) Bangerth, W.; Hartmann, R.; Kanschat, G. *ACM Trans. Math. Software* **2007**, *33* (4), 24.
- (47) Wickham, J. N.; Herhold, A. B.; Alivisatos, A. P. *Phys. Rev. Lett.* **2000**, *84* (5), 923–926.
- (48) Grünwald, M.; Dellago, C. *Nano Lett.* **2009**, *9* (5), 2099–2102.
- (49) Xu, Q.; Huang, B.; Zhao, Y.; Yan, Y.; Noufi, R.; Wei, S.-H. *Appl. Phys. Lett.* **2012**, *100* (6), -.
- (50) Zhao, Y.; Pan, H.; Lou, Y.; Qiu, X.; Zhu, J.; Burda, C. *J. Am. Chem. Soc.* **2009**, *131* (12), 4253–4261.
- (51) Xie, Y.; Riedinger, A.; Prato, M.; Casu, A.; Genovese, A.; Guardia, P.; Sottini, S.; Sangregorio, C.; Miszta, K.; Ghosh, S.; Pellegrino, T.; Manna, L. *J. Am. Chem. Soc.* **2013**, *135* (46), 17630–17637.
- (52) Luther, J. M.; Jain, P. K.; Ewers, T.; Alivisatos, A. P. *Nat. Mater.* **2011**, *10* (5), 361–366.
- (53) Caldwell, A. H.; Ha, D.-H.; Ding, X.; Robinson, R. D. Analytical modeling of localized surface plasmon resonance in heterostructure copper sulfide nanocrystals. *J. Chem. Phys.* **2014**, *141*, 164125.